Astronomy & Astrophysics manuscript no. amirocha
July 18, 2019
©ESO 2019

Signatures of UV radiation around low-mass protostars in the Serpens Main with IRAM 30m

Agnieszka Mirocha[1,2], Agata Karska[2], Lars E. Kristensen[3], Marcin Gronowski[4], Miguel Figueira[5], Marcin Gładkowski[2,6], Michał Żółtowski[2], and Łukasz Tychoniec[7]

[1] Astronomical Observatory of the Jagiellonian University, ul. Orla 171, 30-244 Kraków, Poland
e-mail: amirocha@doctoral.uj.edu.pl
[2] Centre for Astronomy, Faculty of Physics, Astronomy and Informatics, Nicolaus Copernicus University, ul. Grudziądzka 5, 87-100 Toruń, Poland
[3] Centre for Star and Planet Formation, Niels Bohr Institute and Natural History Museum of Denmark, University of Copenhagen, Øster Voldgade 5-7, DK-1350 Copenhagen K, Denmark
[4] Faculty of Physics, University of Warsaw, ul. Pasteura 5, 02-093 Warszawa, Poland
[5] National Centre for Nuclear Research, ul. Pasteura 7, 02-093 Warszawa, Poland
[6] Nicolaus Copernicus Astronomical Center, ul. Rabiańska 8, 87-100 Toruń, Poland
[7] Leiden Observatory, Leiden University, P.O. Box 9513, NL-2300RA Leiden, The Netherlands

Received [Month] [Day], 2019; accepted [Month] [Day], 2019

ABSTRACT

Context. The Serpens Main is one of the most studied star forming region containing low-mass protostars. Observations at submillimetre range allow to determine physical and chemical processes around young stellar objects.
Aims. We aim to characterise the UV radiation in the surroundings of the low-mass protostars. We analyse the exitation and spatial extent of HCN, CN, CS and their isotopologues to identify the underlying processes. We can investigate the feedback from protostars and the excitation mechanisms of molecules.
Methods. We present 30 arcmin^2 IRAM 30m maps of CN $J = 1 - 0$, HCN $J = 1 - 0$, and CS $J = 3 - 2$ encompassing 10 Class 0/I protostars. We calculate HCN and CN column densities toward protostars and selected outflows positions. The column densities are compared with the Nahoon astrochemical model of molecules abundaces in order to characterise UV radiation field.
Results. Emission of HCN $J = 1 - 0$ and CS $J = 3 - 2$ is co-spatial with outflows, whereas CN emission peaks at the positions of protostars. CN and HCN column densities are of the order of 10^{13}-10^{14}cm^{-2}. Regardless of gas parameters, CN/HCN column density ratio is 1-10. This result can be reproduced by providing an additional UV radiation source of 0.001 to 0.044 G_0.
Conclusions. The UV radiation field is significantly higher in the closest distances from protostars. The astrochemical model shows that an additional source of UV radiation is needed to cover the abundances range indicated by observations.

Key words. astrochemistry – stars: formation – ISM: molecules – ISM: individual objects: Sepens Main – Submillimeter: ISM

1. Introduction

Low-mass stars are the most numerous objects among stellar population in galaxies (Kroupa (2002)). At first stages of star formation protostars are formed inside molecular cloud, surrounded by massive envelopes exceeding for 10^4 AU in diameter (Lada (1987); Larson (2003); Bergin & Tafalla (2007)). The embedded phases of low-mass star formation (Class 0/I YSOs, Andre et al. (1993)) is characterised by gas and dust accretion from an envelope and bipolar, collimated outflows which carry out molecular gas from the dense core (Zuckerman et al. (1976), Arce & Sargent (2006)).

Molecular outflows properties are typically traced by low-J CO transitions (Bontemps et al. (1996), Dunham et al. (2014)). Herschel-PACS observations of the high-J CO emission around low-mass protostars showed the presence of a warm component about $T_{\rm rot}$ 300 K, hot component of $T_{\rm rot}$ 600 – 800 K (Karska et al. (2013), Green et al. (2013)) and very hot component exceeding 1000 K for some sources (Manoj et al. (2013)). The high-temperature CO emission can be explained as shocked-heated gas created by UV-irradiated shocks (Kristensen et al. (2017)). Shock waves are created in the inner part of accretion disk where the gas is heated by the 10,000 K radiation filed (Spaans et al. (1995)). UV photons propagate in low-density outflow cavities for large distances, modifying the chemical composition of low-mass neighbourhood.

Previous studies of energetic processes around low-mass protostars showed observational premises of the influence of UV radiation on molecules. At protostars positions was observed higher emission of [C I] than in off-source positions what brought to conclusion of photodissociation CO (van Kempen et al. (2009)). The fluxes of [OI] and [CII] are significantly higher than fully-shielded C-shock models (Karska et al. (2018)). The other photodissociation tracer H_2O/OH showed a few order of magnitude disagreement with shock models (Karska et al. (2014)). Therefore, ultraviolet radiation may play an important role in low-mass protostars surroundings.

The relative abundance of CN and HCN molecules is widely used a tracer of UV radiation in different astronomical context (e.g. Fuente et al. (1995), Chapillon et al. (2012), Riaz et al.

(2018)). CN is a product of photodissociation of HCN with the photodissociation rate of 1.64×10^{-9}. CN has smaller photodissociation rate of 5.19×10^{-10} (Heays et al. (2017)), thus is not that sensitive for photodissociation as HCN. Since CN and HCN can be photodissociated selectively, therefore the CN/HCN ratio probes regions affected by UV radiation. The ratio is the highest near the source of the UV emission, and decreases with the distance from the source (Fuente et al. (1993)). Tracing the physical and chemical processes dominated by UV radiation lead to better understanding of the protostellar evolution. Ultraviolet radiation can propagate in large scales of 1000 AU (Kristensen et al. (2017)), changing the properties of the surrounding matter. Since the UV radiation around low-mass protostars was studied only in the source position (Stäuber et al. (2007), Riaz et al. (2018)) or in the source closest neighbourhood (Hogerheijde et al. (1999), Bachiller et al. (2001), **?**), the spatial extend of UV fields in larger scales is the matter of question. We address the following questions in our paper: How does the UV radiation affect the low-mass surrounding? Where the molecules are dissociated? What is the spatial extend of the UV fields? What is the typical UV radiation around Class 0/I protostars?

We present the CN, HCN, CS and their isotolopologues molecular data observed in the Serpens Main star forming region. Section 2 contains the overview of the observations and the targeted sample. The results derived from the observations are shown in the Section 3, while further analysis of the data in Section 4. In the section 5 we refer to the previous studies of the topic and provide the discussion of the results. The summarising Section 6 is closed with our conclusions.

2. Observations

2.1. IRAM data and reduction process

The Serpens Main star forming region was observed with IRAM 30 between 14 and 17 July 2009 (project no. xxx, PI: L. Kristensen). We used the Eight MIxer Receiver (EMIR) as the frontend. The observations were performed in the EMIR bands E090 (molecule HCN $J = 1-0$) covering the range 73-117 GHz and E150 (molecules CN $J = 1-0$ and CS $J = 3-2$) covering the frequencies between 125 and 184 GHz. Due to the EMIR receiver wide bands additional molecular lines of $C^{34}S$ $J = 3-2$, $H^{13}CN$ $J = 1-0$ and $H^{13}CN$ $J = 2-1$ were also observed. The backend was the Versatile SPectrometer Array (VESPA) autocorrelator and the 1 MHz filterbank reaching the spectral resolution of 39 kHz (E150 band) and 78 kHz (E090 band). The telescope beam size varies from 14″ at 172.68 GHz to 29″ at 86.34 GHz (Table 1). The antenna temperatures were converted to main-beam brightness temperature T_{MB} using the main beam efficiency according to the expresion: $T_{MB} = T_A/\eta_{MB}$. The exact upper levels enegies, line frequencies, beam sizes and beam efficiencies are given in Table 1. Observations included scans of the Ser-SMM1 (centered at $\alpha_{J2000} = 18^h29^m49.6^s$, $\delta_{J2000} = +01°15'20.5''$ with $V_{LSR} = +8.5$ km/s) and the Ser-SMM3/Ser-SMM4 (centered at $\alpha_{J2000} = 18^h29^m56.6^s$, $\delta_{J2000} = +01°14'00.3''$ with $V_{LSR} = +7.6$ km/s) regions, both 1′×3′ OTF maps. The size of the maps is about 300″ × 350″, covering both Ser-SMM1 and Ser-SMM3/Ser-SMM4 regions. The regions are referenced in the article as 'the Northen part' and 'the Southern part' respectively.

Data reduction was carried out with the CLASS package within GILDAS[1]. Each spectrum was corrected for the baseline shape, the spike channels were removed and the velocity was resampled to a resolution of 0.5 km/s. The baseline fitting of the order of 0 was sufficient for our observations. The rms of extracted spectra values vary from 0.024 K to 0.125 K. Both OTF maps were merged in one map covering 300×350 arcsec. The spectra obtained were exported from the CLASS package and analysed with Python scripts.

[1] See http://www.iram.fr/IRAMFR/GILDAS

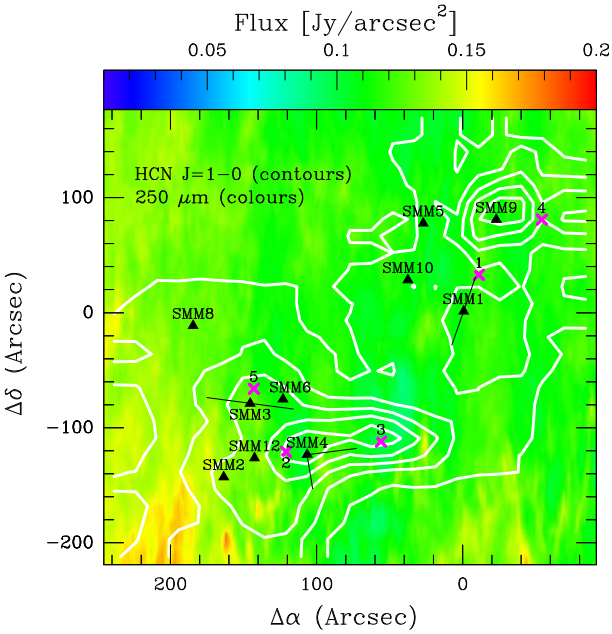

Fig. 1. Molecular emission of HCN J=1-0 (contours) overplot on continuum emission *Herschel*/SPIRE (Griffin et al. 2010) 250 μm (colours). Countours the lowest level is set on 0.4 K km/s (30 σ), step size of 4 K km/s.

2.2. Continuum emission

2.3. Physical properties of embedded protostars

Ten Class 0/I protostars are present in the observed region. There are deeply embedded sources so the radiation coming from theirs neighbourhood is highly absorbed in the envelopes, then re-emitted in the IR range. Envelopes become thinner with time due to outflow-envelope interactions (Arce & Sargent (2006)). Class I sources SEDs are dominated by the emission in shorter wavelengths in respect to Class 0 objects. Thus Spectral Energy Distributions (SEDs) allow to estimate the evolutional stage of an object (Andre et al. (1993)).

Figure A.1 shows spectral energy distributions for all Class 0/1 protostars in the region (Table 2). The SED plots include the selected literature samples (Dunham et al. (2015)) combined with the data from the Herschel Gould Belt survey project (André et al. (2010)). The additional Herschel data cover the SED peak, therefore provide a more detailed information allowing to calculate the bolometric temperatures and luminosities of the protostar more precisely.

Table 2 contains the observed protostars parameters as well as the classification from Enoch et al. (2009). Early Class 0 was defined as a protostar of bolometric temperature lesser than 50 K. Prostostars characterised by bolometric temperature between 50 K and 100 K were classified as Late Class 0 protostars. Class I protostars were divided for Early and Late sub-type by the bolometric temperature of 300 K.

Table 1. Overview of the observations

Mol.	Trans.	ν [a] [K]	E_u/k_B [a] [GHz]	A_{ul} $[s^{-1}]$	g	n_{crit} $[cm^{-3}]$	Beam size ($''$)	Beam eff. η_{MB}
HCN	1-0	88.631602	4.25	2.407×10^{-5} [b]	3	5.0×10^6 [d]	28	0.81
CN	1-0	113.494921	5.45	1.182×10^{-5} [b]	3	1.1×10^5 [e]	22	0.78
CS	3-2	146.969029	14.1	6.071×10^{-5} [b]	7	2.6×10^5 [e]	16	0.74
$C^{34}S$	3-2	144.617109	13.9	5.77×10^{-5} [c]	7	no data	16	0.74
$H^{13}CN$	1-0	86.342274	4.14	no data	3	9.7×10^6 [d]	29	0.81
$H^{13}CN$	2-1	172.677881	12.43		5	1.2×10^6 [e]	14	0.68

References: [a]JPL database; [b]LAMDA database; [c]Chandra et al. 1995; [d]Jiménez-Donaire et al. 2016, assuming optically thin transition lines for an excitation temperature of 20K; [e]Shirley 2015, assuming optically thin transition lines for an excitation temperature of 50K.

Notes. Beam sizes and efficiencies are taken from http://www.iram.es/IRAMES/mainWiki/Iram30mEfficiencies

Most of the observed protostars in the Serpens Main region are very young, embedded sources of Early Class 0. SMM4, SMM10 and SMM12 are classified as Late Class 0 YSOs. The SMM5 and SMM6 protostars are the most evolved objects in our sample (Class I).

3. Results

3.1. Molecular emission maps

The line maps in the targeted molecules show variety of structures that can be associated with YSOs and a large-scale cloud emission. Different spatial extend in molecules radiation is connected with various physical conditions around protostars. Here, we present the large-scale maps of CS $J = 3-2$, HCN $J = 1-0$ and CN $J = 1-0$. Maps of their isotopologues are shown in the Appendix A.

Outflows associated with low-mass protostars (Table 2) are observed in certain molecules emission. Blue- and redshifted molecular outflows around Ser-SMM1, Ser-SMM3 and Ser-SMM4 were pointed based on CO $J = 6-5$ and CO $J = 3-2$ observations (Yıldız et al. (2015)). Additionally, five outflows positions were selected to more detailed studies (Table 3).

The integrated line intensity map of HCN $J = 1-0$ (Fig. 2) shows extended emission along outflow directions. The HCN $J = 1-0$ line was detected at all positions, although it is weak at the positions of Ser-SMM5 and Ser-SMM10. On the other hand, the HCN $J = 1-0$ emission is particularly strong around Ser-SMM4 and Ser-SMM9 sources. The emission maxima are detected among the known outflows of Ser-SMM1 and Ser-SMM4 (Yıldız et al. (2015)). Especially, at the end of Ser-SMM4 blue outflow (position no. 4) we have significantly strong maximum of the HCN $J = 1-0$. There is no intensively elongated outflow structure from Ser-SMM3 source.

CS $J = 3-2$ line emission map (Fig. 3) shows similar spatial distribution to HCN $J = 1-0$. The most significant elongated structure can be associated with Ser-SMM4 blue-shifted outflow. It is situated at the same place in both maps, extending over 80$''$. A similar large-scale structure is detected along Ser-SMM1 outflows, although it is much more distinctive in the HCN $J = 1-0$ map. A strong emission around Ser-SMM9 have a circular shape in HCN $J = 1-0$ map, however, it has more elongated structure in CS $J = 3-2$ line emission which overlaps with the S68N outflows (Kristensen et al. (2010)). The peaks of emissions are situated in the different places. HCN $J = 1-0$ has relatively strong emission around Ser-SMM4 protostar, but in CS $J = 3-2$ line a significant emission towards position no. 3 can be noticed that indicates CN $J = 1-0$ local maximum.

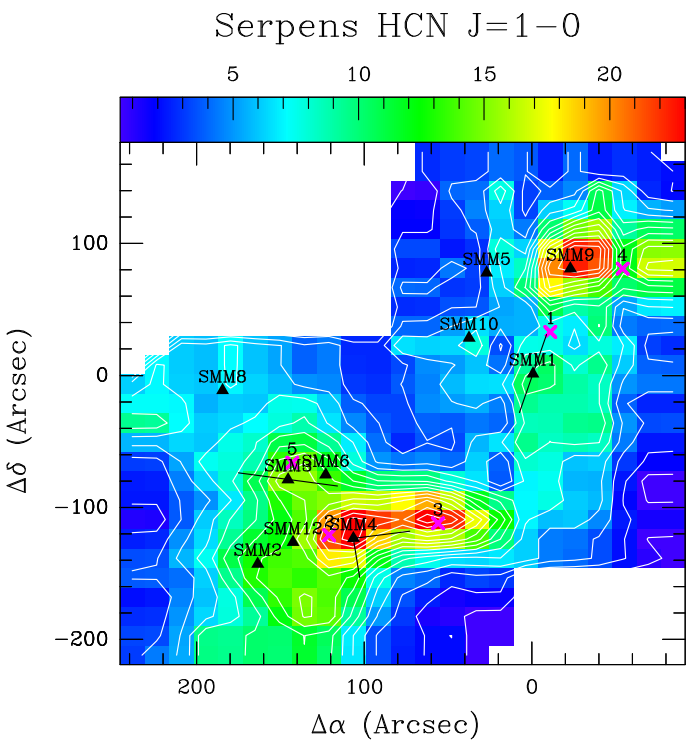

Fig. 2. Emission of the HCN $J = 1-0$ in the Serpens Main region. Black triangles show the positions of the protostars (Suresh et al. (2016)), whereas the black lines show the associated outflow directions (Yıldız et al. (2015)). Outflow positions were displayed as pulrple crosses.

CN $J = 1-0$ line emission is focused mostly around the positions of protostars (Fig. 4). The highest local peaks are associated with Class 0 low-mass protostars: Ser-SMM1 (8.2 K km/s), Ser-SMM3 (15.9 K km/s), Ser-SMM4 (14.1 K km/s) and Ser-SMM6 (15.3 K km/s). The spatial distribution is qualitatively different compared to the HCN $J = 1-0$ map. The strongest emission characterises the dense surroundings of Ser-SMM3, Ser-SMM6 and Ser-SMM4 sources while the northern part of this region does not show such a distinct emission in the HCN $J = 1-0$ line. On the other hand, dense emissive region of the Ser-SMM9 source is significantly weaker in CN $J = 1-0$ line. CN $J = 1-0$ map can be characterised by compact, condensed

Table 2. Catalogue of protostars properties

Source (J2000.0)	R.A. (J2000.0)	Decl.	T_{bol} (K)	L_{bol} ($L_\odot$)	Class	Other names
SMM9	18 29 48.3	+01 16 42.7	34.9	10.3	Early Class 0	ISO241, WMW23
SMM1	18 29 50.0	+01 15 20.3	35.4	78.7	Early Class 0	FIRS1, Ser-emb6, Bolo23, EC41
SMM5	18 29 51.4	+01 16 38.3	150.5	3.7	Early Class I	EC53, WMW24, Ser p3
SMM10	18 29 52.3	+01 15 48.8	82.6	6.2	Late Class 0	WMW21
SMM4	18 29 57.0	+01 13 11.3	76.9	4.4	Late Class 0	
SMM6	18 29 57.8	+01 14 05.3	532.3	43.1	Late Class I	EC90, WMW35, SVS20S
SMM12	18 29 59.1	+01 13 14.3	96.9	5.7	Late Class 0	
SMM3	18 29 59.6	+01 13 59.2	35.0	6.9	Early Class 0	
SMM2	18 30 00.5	+01 12 57.8	30.5	4.07	Early Class 0	Ser-emb4, Bolo28
SMM8	18 30 01.9	+01 15 09.2	15.3	0.2	Early Class 0	

Coordinates taken from Suresh et al. 2016, except SMM8 (Lee et al. 2014).

Table 3. Properties of the selected off-source positions

Pos.	R.A. (J200)	Decl. (J200)	Remarks
1	18:29:45.47	+01:15:53.5	SMM1 blue-shifted outflow in CO $J = 3-2$
2	18:29:54.66	+01:13:19.5	max. CN $J = 1-0$, SMM4 blue-shifted outflow in CO $J = 3-2$
3	18:29:50.33	+01:13:68.5	max. HCN $J = 1-0$, SMM4 blue-shifted
4	18:29:43	+01:16:41.5	outflow visible in $C^{34}S$(3-2)
5	18:29:56.13	+01:14:14.5	max. CN $J = 1-0$, SMM9 surroundings

emission without any strongly elongated structures. The $H^{13}CN$ $J = 1-0$ line exhibits similar morphological distribution as CN(1-0) and $C^{34}S$(3-2).

In the presence of the UV radiation, HCN molecule photodissociates into CN molecule and H atom (Stäuber et al. (2005)). Thus, combined map of these molecules can indicate regions with stronger UV radiation. We present a large-scale map of CN $J = 1-0$ to HCN $J = 1-0$ flux ratio (Fig. 5). The image of CN emission has been resampled to beam size of HCN in order to compare the same emitting regions. CN/HCN ratio is relatively low around the brightest submillimetre source Ser-SMM1. Similarly, at the dense area of Ser-SMM9 surrounding a significantly weaker CN/HCN emission can be noticed. On the other hand, it peaks at the Northern part of the map around rather faint Ser-SMM5 source. At the Southern part high CN/HCN ratio emission is more extended than in the Northen part. It expands from Ser-SMM3 and Ser-SMM6 area to the North. High CN/HCN ratio can also be found on the edges of the image but it is probably caused by different size of the CN and the HCN maps.

The low energy level of HCN (E_u = 4.25 K) traces cold, high-density gas. HCN has previously been shown to be a good tracer of molecular outflows activity (Walker-Smith et al. (2014)). Similar spatial distribution is presented in the CS map. It means that both species trace the gas of the same properties. The CN line is similarly low-energetic, however it peaks in different areas than HCN and CS. CN as a product of HCN photodissotiation indicates other properties of low-mass protostars surroundings (Section 4).

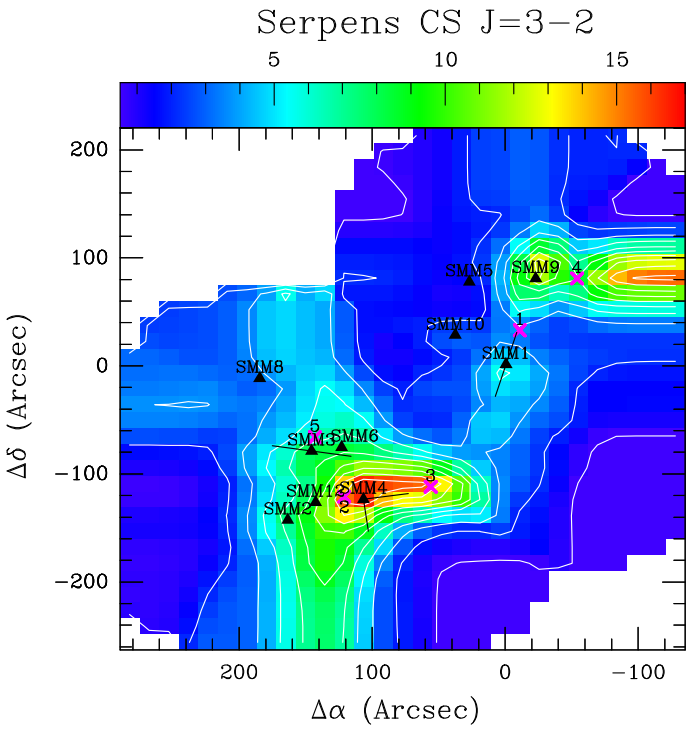

Fig. 3. Similar to Fig. 2 but the emission of the CS $J = 3-2$ line.

To summarise, spatial distribution of different lines emission varies depending on the observed molecule. The most distinct differences can be noticed between HCN and CN map. Most of the sources show high flux values in both molecules (Table 4). However, they present unequal levels which indicates regions of different properties. In order to better understand this issue we analyse the molecular line profiles in the Section 3.2.

3.2. Line profiles

We selected 14 representative on-source and off-source positions for a detailed analysis (Fig. 6). Nine of them are corresponding to the protostars positions, the other five off-source positions were selected based on local maximum of the flux.

The mean region is consistent with HCN $J = 1-0$ beam size (27.8") for all molecules. In the majority of our sources five of targeted lines were detected: CN $J = 1-0$, HCN $J = 1-0$, CS $J = 3-2$, $C^{34}S$ $J = 3-2$ and $H^{13}CN$ $J = 1-0$. The line is

Table 4. Integrated fluxes of the observed line at the positions of protostars

Source	Line	Flux (K)	Column dens. (cm^{-2})
SMM1	CN 1-0	6.53	1.3×10^{15}
	HCN 1-0	6.78	1.9×10^{14}
	CS 3-2	6.93	7.9×10^{13}
	$C^{34}S$ 3-2	1.39	1.7×10^{13}
	$H^{13}CN$ 1-0	1.28	no data
	$H^{13}CN$ 2-1	0.03	no data
SMM2	CN 1-0	10.58	2.2×10^{15}
	HCN 1-0	13.98	4.0×10^{14}
	CS 3-2	8.03	9.1×10^{13}
	$C^{34}S$ 3-2	1.15	1.4×10^{13}
	$H^{13}CN$ 1-0	2.46	no data
	$H^{13}CN$ 2-1	not detected	
SMM3	CN 1-0	13.26	2.7×10^{15}
	HCN 1-0	12.48	3.6×10^{14}
	CS 3-2	10.04	1.1×10^{14}
	$C^{34}S$ 3-2	0.37	4.4×10^{12}
	$H^{13}CN$ 1-0	0.98	no data
	$H^{13}CN$ 2-1	not detected	
SMM4	CN 1-0	13.06	2.7×10^{15}
	HCN 1-0	20.20	5.7×10^{14}
	CS 3-2	19.81	2.2×10^{14}
	$C^{34}S$ 3-2	0.02	1.9×10^{11}
	$H^{13}CN$ 1-0	2.10	no data
	$H^{13}CN$ 2-1	0.26	no data
SMM5	CN 1-0	2.57	3.2×10^{14}
	HCN 1-0	3.71	1.1×10^{14}
	CS 3-2	2.33	5.2×10^{13}
	$C^{34}S$ 3-2	0.07	7.9×10^{11}
	$H^{13}CN$ 1-0	0.70	no data
	$H^{13}CN$ 2-1	not detected	
SMM6	CN 1-0	11.48	2.4×10^{15}
	HCN 1-0	11.85	3.4×10^{14}
	CS 3-2	9.37	1.1×10^{14}
	$C^{34}S$ 3-2	0.54	6.4×10^{12}
	$H^{13}CN$ 1-0	0.16	no data
	$H^{13}CN$ 2-1	0.02	no data
SMM9	CN 1-0	4.82	9.9×10^{14}
	HCN 1-0	12.55	3.1×10^{14}
	CS 3-2	13.75	1.7×10^{14}
	$C^{34}S$ 3-2	1.17	1.4×10^{13}
	$H^{13}CN$ 1-0	1.61	no data
	$H^{13}CN$ 2-1	0.04	no data
SMM10	CN 1-0	2.89	5.9×10^{14}
	HCN 1-0	4.40	1.3×10^{14}
	CS 3-2	4.47	5.1×10^{13}
	$C^{34}S$ 3-2	0.35	4.2×10^{12}
	$H^{13}CN$ 1-0	0.98	no data
	$H^{13}CN$ 2-1	not detected	
SMM12	CN 1-0	10.58	2.2×10^{15}
	HCN 1-0	13.98	4.0×10^{14}
	CS 3-2	10.30	1.2×10^{14}
	$C^{34}S$ 3-2	0.93	1.1×10^{13}
	$H^{13}CN$ 1-0	2.46	no data
	$H^{13}CN$ 2-1	not detected	

a Line frequency at the main peak position.
b Integrated flux above 3σ.

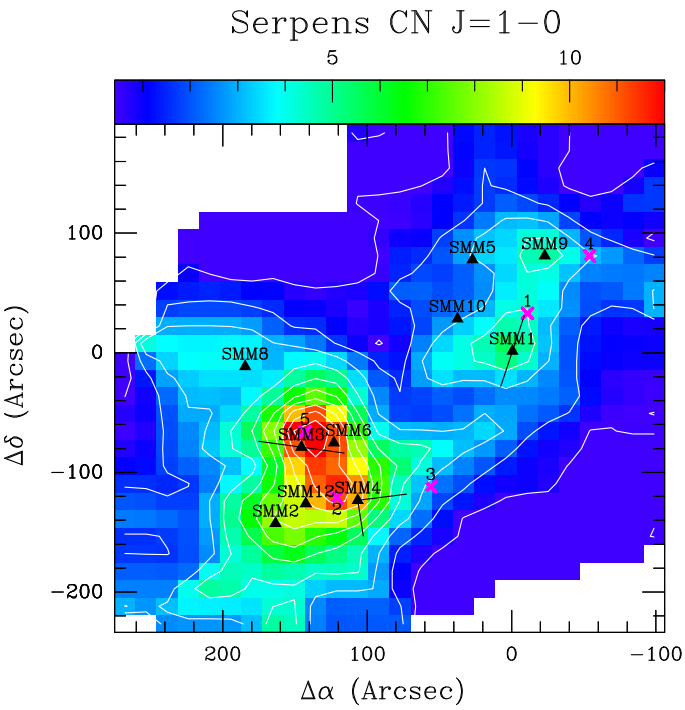

Fig. 4. Similar to Fig. 2 but the emission of the CN $J = 1 - 0$ line.

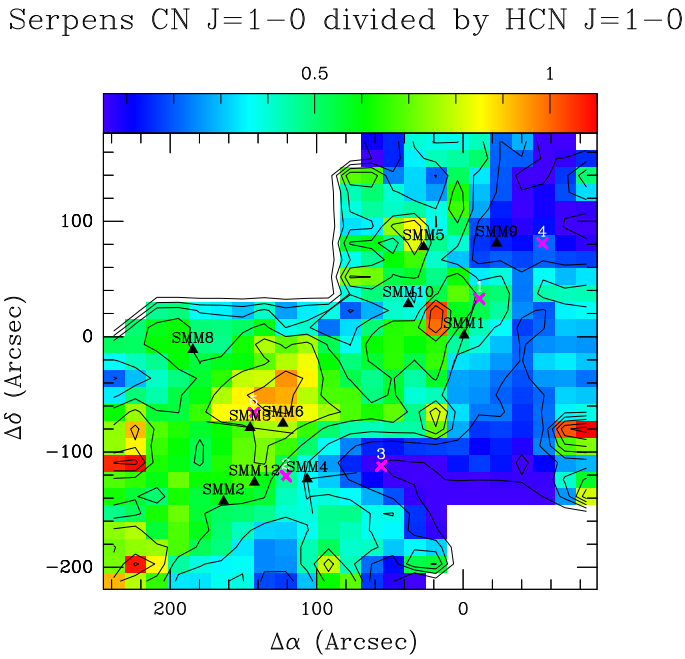

Fig. 5. Emission of the divided fluxes CN $J = 1 - 0$/HCN $J = 1 - 0$ in the Serpens Main region. Black triangles show the positions of the protostars (Suresh et al. 2016), whereas the black lines show the associated outflow directions (Yıldız et al. 2015). Outflow positions were displayed as pulrple crosses.

considered to be detected if there is an emission at the level of at least 3σ. A weak emission from $H^{13}CN$ $J = 2 - 1$ was found at the positions of four sources and it is not included in the Figure.

The strongest emission occurs in HCN $J = 1 - 0$, CN $J = 1 - 0$ and CS $J = 3 - 2$ lines and it was detected at the position of all of the sources. The emission in the other lines was multiplied in order to compare profiles between different molecules. In HCN, CN species and their isotopologues a few different velocity components can be identified what indicates the hyperfine splitting. This occurs if a molecule has a non-zero nuclear spin so there is also an interaction between the nuclear spin and the electronic angular momentum. The most distinct splitting can be spotted in the CN $J = 1 - 0$ profiles with five separate components situated between -70 km/s and 18 km/s. The HCN $J = 1 - 0$ line is characterised by three components with low separation situated in the range of -2 km/s – 16 km/s.

Ser-SMM1, Ser-SMM9, and Ser-SMM10 sources have wide spectral lines, while others exhibit narrow line profiles. Spectra extracted form Positions no. 1, 4 and 5 shows prominent blue-shifted wings what can be associated with outflows. Similar structure can be noticed in the Ser-SMM3 (panel no. 7) CS 3-2 and HCN $J = 1 - 0$ profiles.

4. Analysis

4.1. Lines column densities

Table 4 shows fluxes integrated from the average line profile at the positions of known protostars. Flux calculation in individual lines allows us to determine the column density of a given transition. The column density of the upper level $N_{\rm up}$ of each observed line was calculated based on following relation:

$$N_u = \beta \frac{\nu W}{A} \tag{1}$$

where $\beta = 1937$ cm^{-2} and $W = \int T_{mb}\, dV$ is the integrated intensity of the emission line. The frequency ν should be given in GHz.

The column densities of the upper level of CN $J = 1 - 0$ and HCN $J = 1 - 0$ transitions are presented in Table 4. In the closest surroundings of low-mass protostars CN $J = 1 - 0$ is stronger than the lowest transition line of HCN. The column density of CN $J = 1 - 0$ varies between 10^{14} -10^{15} cm^{-2}, while in the column density of the HCN's lowest transition reaches 10^{14} cm^{-2} . Except for the Ser-SMM9 and the Ser-SMM10 neighbourhood, HCN $J = 1 - 0$ line column density is an order of magnitude lower than the column density of the equivalent CN transition. This result provides a clue to better understand of the low-mass protostars chemistry.

4.2. RADEX modelling

Molecules column densities can be independently determined using molecular excitation models. Line ratio can provide additional information concerning physical properties of the observed gas.

The non-LTE radiative transfer code RADEX (citevdT07) was run in order to prepare sets of molecular excitation models. The CN and HCN molecules column density ratio was the only free parameter. HCN column density was chosen as 10^8 cm^{-2} in order to ensure optically thin emission. CN column density parameter varies from 10^6 cm^{-2} to 10^{10} cm^{-2} what translates into $N_{\rm CN}/N_{\rm HCN}$ in following limits: 10^{-2}-10^2. The sets of models were developed assuming a line width of 1.0 km s^{-1}, hydrogen densities of $n_{\rm H_2} = 10^3$ cm^{-3}, $n_{\rm H_2} = 10^4$ cm^{-3} and $n_{\rm H_2} = 10^5$ cm^{-3} and kinetic temperatures of $T_{\rm kin} = 30$ K, $T_{\rm kin} = 75$ K and $T_{\rm kin} = 200$ K. The molecular data files used during modelling were procured from the Leiden Atomic and Molecular Database (LAMDA, Schöier et al. (2005)).

Fig. 7 presents one exemplary set of models of CN/HCN column density ratio versus the modelled line intensities ratio for

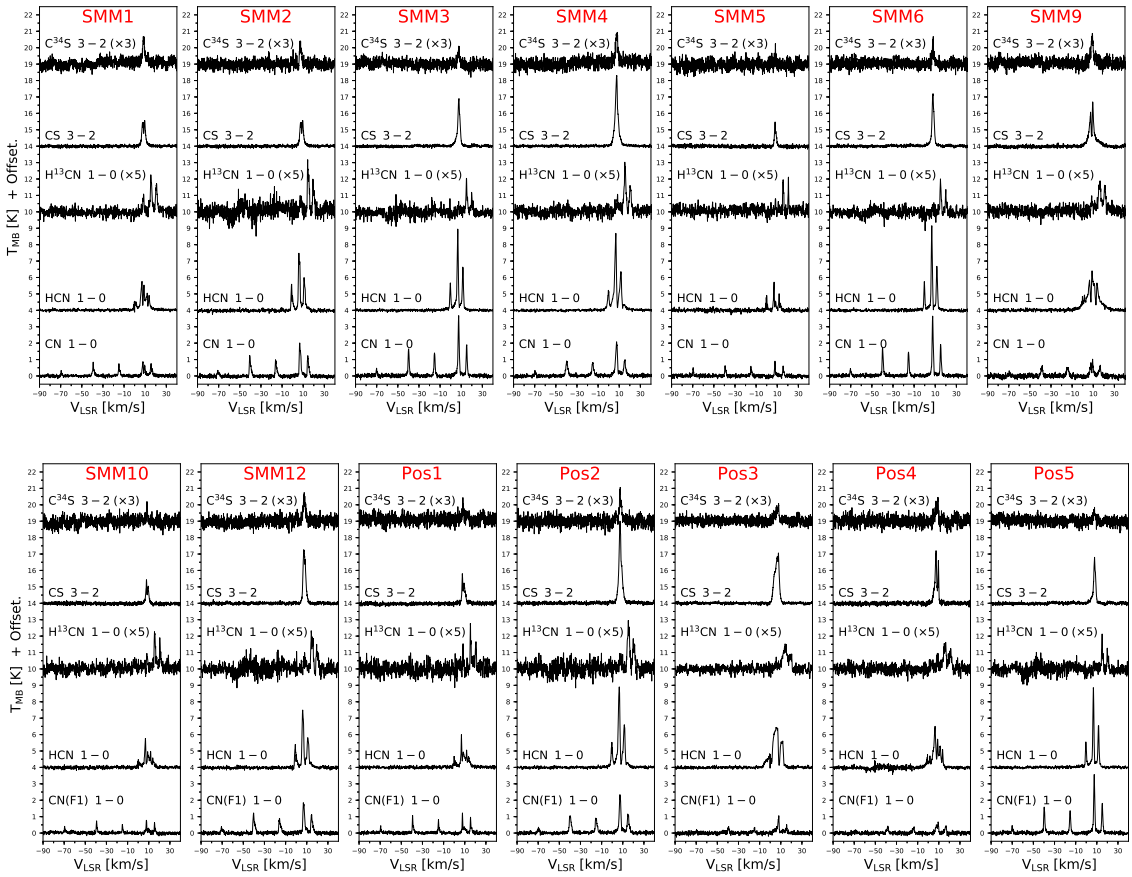

Fig. 6. Serpens Main sources spectra of $C^{34}S$ $J = 3-2$, CS $J = 3-2$, $H^{13}CN$ $J = 1-0$, HCN $J = 1-0$ and CN $J = 1-0$ lines.

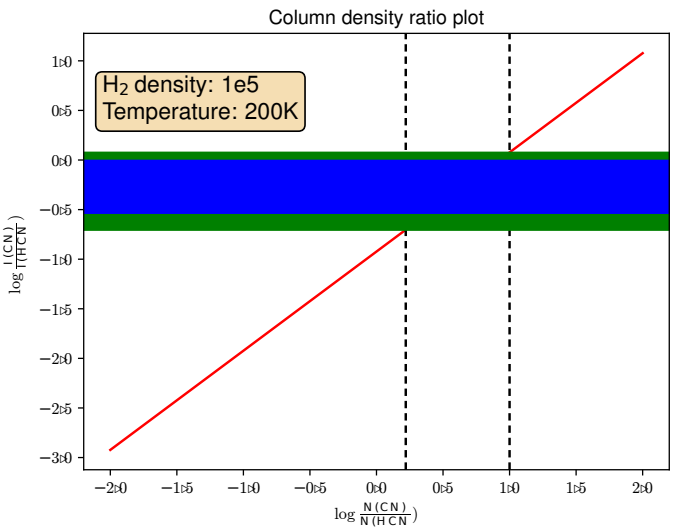

Fig. 7. RADEX model predictions for the CN/HCN column density ratio for hydrogen densities of $n_{H_2} = 10^5$ cm^{-3} and kinetic temperatures of $T_{kin} = 200$ K (red line). The observed line intensity ratio is plotted in blue (protostars positions) and green (all positions).

hydrogen densities of $n_{H_2} = 10^5$ cm^{-3} and kinetic temperatures of $T_{kin} = 200$ K. The rest of the models are shown in the Appendix B. CN/HCN column density ratio weakly depends on hydrogen density and kinetic temperature in the low limit of those parameters. All presented models show similar properties.

Table 5. RADEX calculations of CN/HCN column density ratio

n_{H_2} [cm^{-3}]	T_{kin} [K]	$\log_{10}$(N[CN]/N[HCN])
10^3	30	0.03-0.88
10^3	75	0.06-0.84
10^3	200	0.00-0.78
10^4	30	0.16-0.94
10^4	75	0.08-0.86
10^4	200	0.04-0.82
10^5	30	0.20-0.98
10^5	75	0.18-0.86
10^5	200	0.22-1.00

The modelled line intensities are compared with the observations. The observed line intensity ratio covers a range of 0.0-1.0 of the column density ratio in the logarithmic scale. That corresponds to a few times higher CN column density than the same parameter of HCN. This result slightly depends on hydrogen densities and kinetic temperature of the gas (see Table 5).

The sets of models shown in this section indicate that CN/HCN column density ratio covers the range of 1-10 regardless of excitation conditions. This result suggests that the UV radiation may play an important role around low-mass protostars.

4.3. Astrochemical model

In Section 4.2 we have raised a question about influence of the UV radiation on the surrounding of the observed sources. A sim-

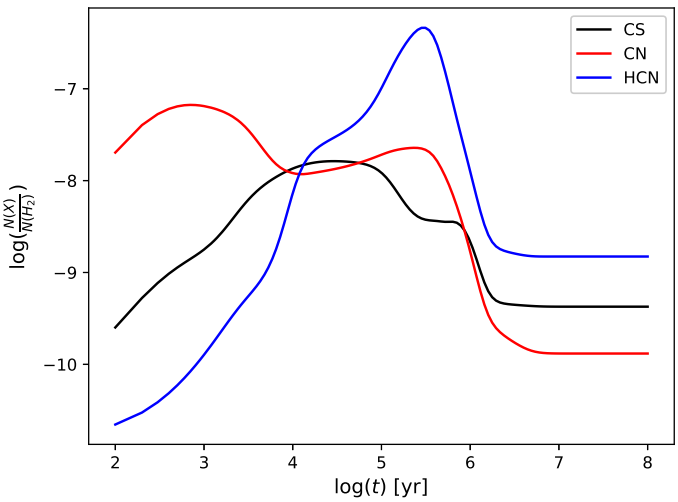

Fig. 8. Time evolution of CN (red line), HCN (blue line) and CS (black line) abundances obtained with Nohoon astrochemical code with initial parameters of $n_{\mathrm{HI+H_2}} = 10^4$ cm^{-3}, $T = 10$ K, $A_{\mathrm{V}} = 5^{\mathrm{m}}$. The other parameters remained defaulted: cosmic-ray ionization rate of 1.3×10^{17} s^{-1}, dust to gas mass ratio of 0.01, dust grain radius of 10^{-5} cm, grain density of 3 g cm^{-3}.

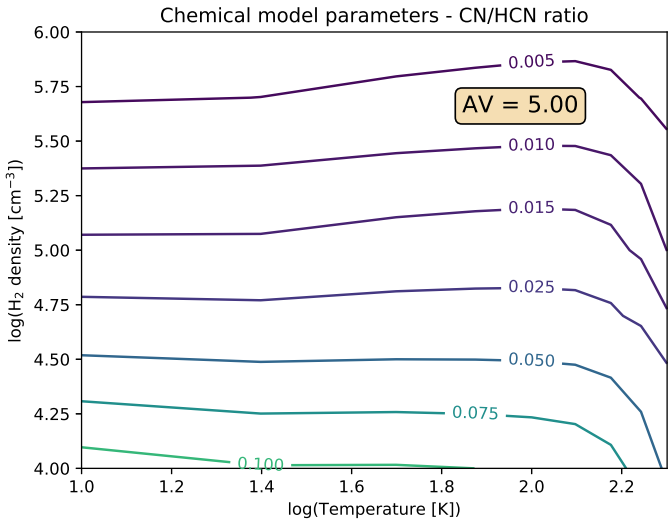

Fig. 9. Contour plot of Nahoon sets of models of CN/HCN abudances ratio with fixed visual extinction $A_{\mathrm{V}} = 5^{\mathrm{m}}$ at the time of 1.063×10^7 yrs after star formation began in the cloud. The other parameters remained defaulted: cosmic-ray ionization rate of 1.3×10^{17} s^{-1}, dust to gas mass ratio of 0.01, dust grain radius of 10^{-5} cm, grain density of 3 g cm^{-3}.

ply astrochemical model can be obtained in order to estimate the intensity of the UV field in reference to units of the interstellar UV field G_0.

HCN easily photodissotiates into CN molecule and H atom. On the other hand, CN needs more energetic photon for disintegration. In the presence of the UV photons HCN can be dissociated, while CN cannot. This leads to higher abundance of CN molecules and increases CN/HCN column density ratio.

We used Nahoon code (Wakelam et al. (2012)) that model the time evolution of 474 species involving gas-phase and gas-grain reactions with fixed temperature, density, UV, and cosmic ray fluxes. The evolution of CN, HCN and CS abundances was started at the time of a dense cloud formation. The UV radiation is described in the code by A_{V} parameter through the relation between visual extinction and the photodissociation rate coefficient:

$$k = \alpha e^{-\gamma A_{\mathrm{V}}} \tag{2}$$

where α and γ are coefficients of the photodissociation process. In case of photodissociation HCN the coefficients equal 1.64×10^{-9} and 3.12 respectively (Heays et al. (2017)).

The first model (Fig. 8) was established for a typical dense cloud with temperature of 10 K and hydrogen total density of $n_{\mathrm{HI+H_2}} = 10^4$ cm^{-3}. The chemical composition of the studied molecules stabilises at the time of 10^7 yrs with HCN higher abundance in respect to CN molecule. We assumed the time of 10^6 yrs as the time when the star formation starts in dense clouds. The modelled abundances of the all 474 species at the time of 10^6 yrs were used as an input data for the following set of models.

In the next models the closest neighbourhood of low-mass protostars was simulated. The initial abundances of all species available in Nahoon code were calculated based on the first model. We adopted the UV radiation and cosmic ray fluxes typical for dense clouds as an initial conditions. The visual extinction and the total cosmic-ray ionization rate were set as 5^{m} and 1.3×10^{17} s^{-1} respectively. The sets of models were run for the temperature range between 10 and 200 K and the total hydrogen

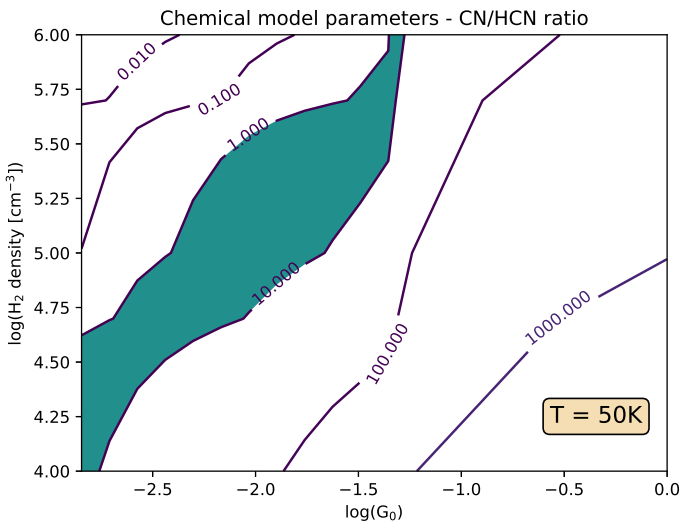

Fig. 10. Contour plot of Nahoon sets of models of CN/HCN abudances ratio with fixed temperature $T = 50$ K at the time of 1.063×10^7 yrs after star formation began in the cloud. The other parameters remained defaulted: cosmic-ray ionization rate of 1.3×10^{17} s^{-1}, dust to gas mass ratio of 0.01, dust grain radius of 10^{-5} cm, grain density of 3 g cm^{-3}. The observational column density ratio is marked with blue colour.

densities from 10^4 cm^{-3} to 10^6 cm^{-3}. The resulting ratio of CN and HCN abundances is shown in Fig. 9. The results are consistent with starless cloud model (Fig. 8). Without any additional source of the UV radiation the HCN is more abundant molecule then CN about 2-3 orders of magnitude. Moreover, the CN/HCN abundances ratio is slightly dependent on gas temperature up to 150 K.

This results justify assumptions for the next set of models. The fixed gas temperature of 50 K was set. The models were run for the range of visual extinction between 1^{m} and 2.1^{m} what corresponds to the UV radiation field of 0.044 to 0.001 G_0. The

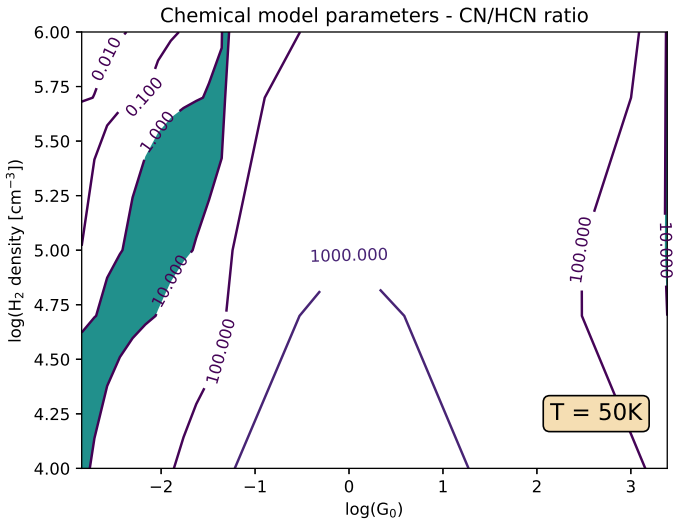

Fig. 11. Contour plot of Nahoon sets of models of CN/HCN abudances ratio with fixed temperature $T = 50$ K at the time of 1.063×10^7 yrs after star formation began in the cloud. The other parameters remained defaulted: cosmic-ray ionization rate of 1.3×10^{17} s^{-1}, dust to gas mass ratio of 0.01, dust grain radius of 10^{-5} cm, grain density of 3 g cm^{-3}. The observational column density ratio is marked with blue colour.

computed CN/HCN abundances ratio is presented in Fig. 11. The additional UV radiation of the strength of few thousandth of the average interstellar UV radiation field is enough to cover the observations in wide range of total hydrogen densities.

An additional source of the UV radiation was needed to reproduce the observational CN/HCN abundances what leads to conclusion that there is non-zero UV radiation field around low-mass protostars.

Acknowledgements. AM, AK and MG are supported by the Polish National Science Center grants 2013/11/N/ST9/00400 and 2016/21/D/ST9/01098. This research has made use of data from the Herschel Gould Belt survey (HGBS) project (http://gouldbelt-herschel.cea.fr). The HGBS is a Herschel Key Programme jointly carried out by SPIRE Specialist Astronomy Group 3 (SAG 3), scientists of several institutes in the PACS Consortium (CEA Saclay, INAF-IFSI Rome and INAF-Arcetri, KU Leuven, MPIA Heidelberg), and scientists of the Herschel Science Center (HSC).

References

André, P., Men'shchikov, A., Bontemps, S., et al. 2010, A&A, 518, L102
Andre, P., Ward-Thompson, D., & Barsony, M. 1993, ApJ, 406, 122
Arce, H. G. & Sargent, A. I. 2006, ApJ, 646, 1070
Bachiller, R., Pérez Gutiérrez, M., Kumar, M. S. N., & Tafalla, M. 2001, A&A, 372, 899
Bergin, E. A. & Tafalla, M. 2007, ARA&A, 45, 339
Bontemps, S., Andre, P., Terebey, S., & Cabrit, S. 1996, A&A, 311, 858
Chapillon, E., Guilloteau, S., Dutrey, A., Piétu, V., & Guélin, M. 2012, A&A, 537, A60
Di Francesco, J., Johnstone, D., Kirk, H., MacKenzie, T., & Ledwosinska, E. 2008, ApJS, 175, 277
Dunham, M. M., Allen, L. E., Evans, Neal J., I., et al. 2015, ApJS, 220, 11
Dunham, M. M., Arce, H. G., Mardones, D., et al. 2014, ApJ, 783, 29
Enoch, M. L., Evans, Neal J., I., Sargent, A. I., & Glenn, J. 2009, ApJ, 692, 973
Enoch, M. L., Glenn, J., Evans, Neal J., I., et al. 2007, ApJ, 666, 982
Evans, Neal J., I., Dunham, M. M., Jørgensen, J. K., et al. 2009, ApJS, 181, 321
Fuente, A., Martin-Pintado, J., Cernicharo, J., & Bachiller, R. 1993, A&A, 276, 473
Fuente, A., Martin-Pintado, J., & Gaume, R. 1995, ApJ, 442, L33
Green, J. D., Evans, Neal J., I., Jørgensen, J. K., et al. 2013, ApJ, 770, 123
Heays, A. N., Bosman, A. D., & van Dishoeck, E. F. 2017, A&A, 602, A105
Hogerheijde, M. R., van Dishoeck, E. F., Salverda, J. M., & Blake, G. A. 1999, ApJ, 513, 350
Karska, A., Herczeg, G. J., van Dishoeck, E. F., et al. 2013, A&A, 552, A141
Karska, A., Kaufman, M. J., Kristensen, L. E., et al. 2018, ApJS, 235, 30
Karska, A., Kristensen, L. E., van Dishoeck, E. F., et al. 2014, A&A, 572, A9
Kristensen, L. E., van Dishoeck, E. F., Mottram, J. C., et al. 2017, A&A, 605, A93
Kristensen, L. E., van Dishoeck, E. F., van Kempen, T. A., et al. 2010, A&A, 516, A57
Kroupa, P. 2002, Science, 295, 82
Lada, C. J. 1987, in IAU Symposium, Vol. 115, Star Forming Regions, ed. M. Peimbert & J. Jugaku, 1
Larson, R. B. 2003, Reports on Progress in Physics, 66, 1651
Manoj, P., Watson, D. M., Neufeld, D. A., et al. 2013, ApJ, 763, 83
Myers, P. C. & Ladd, E. F. 1993, ApJ, 413, L47
Ortiz-León, G. N., Dzib, S. A., Kounkel, M. A., et al. 2017, ApJ, 834, 143
Riaz, B., Thi, W. F., & Caselli, P. 2018, MNRAS, 481, 4662
Schöier, F. L., van der Tak, F. F. S., van Dishoeck, E. F., & Black, J. H. 2005, A&A, 432, 369
Skrutskie, M. F., Cutri, R. M., Stiening, R., et al. 2006, AJ, 131, 1163
Spaans, M., Hogerheijde, M. R., Mundy, L. G., & van Dishoeck, E. F. 1995, ApJ, 455, L167
Stäuber, P., Benz, A. O., Jørgensen, J. K., et al. 2007, A&A, 466, 977
Stäuber, P., Doty, S. D., van Dishoeck, E. F., & Benz, A. O. 2005, A&A, 440, 949
Suresh, A., Dunham, M. M., Arce, H. G., et al. 2016, AJ, 152, 36
van Kempen, T. A., van Dishoeck, E. F., Güsten, R., et al. 2009, A&A, 507, 1425
Wakelam, V., Herbst, E., Loison, J. C., et al. 2012, ApJS, 199, 21
Walker-Smith, S. L., Richer, J. S., Buckle, J. V., Hatchell, J., & Drabek-Maunder, E. 2014, MNRAS, 440, 3568
Wright, E. L., Eisenhardt, P. R. M., Mainzer, A. K., et al. 2010, AJ, 140, 1868
Yıldız, U. A., Kristensen, L. E., van Dishoeck, E. F., et al. 2015, A&A, 576, A109
Zuckerman, B., Kuiper, T. B. H., & Rodriguez Kuiper, E. N. 1976, ApJ, 209, L137

Appendix A: Spectral Energy Distributions

Broad-band observations are needed in order to determine physical properties of a protostar. Dunham et al. 2015 studied properties of protostars in the Serpens molecular cloud using 2MASS (Skrutskie et al. (2006)) and Spitzer IRAC/MIPS (Evans et al. (2009)), observations covering the range of 1.25–70 μm, photometry from Wide-field Infrared Survey Explorer 12 and 22 μm (WISE; Wright et al. (2010)), SHARC-II 350 μm (Suresh et al. (2016)), the SCUBA Legacy Catalog 450 and 850 μm (Di Francesco et al. (2008)) and 1.1 mm observations from Bolocam dust survey (Enoch et al. (2007)). The Serpens Main region was also observed during the Herschel Gould Belt survey project (André et al. (2010)). SPIRE/PACS photometry in the Serpens molecular cloud is discussed in Fiorellino et al. (in prep.).

Based on SEDs the bolometric temperature and luminosity can be calculated for each of the observed protostars. The bolometric luminosity was determined by integrating the SEDs over frequency:

$$L_{bol} = \pi\, d^2 \int F_\nu d\nu \tag{A.1}$$

where d is the cloud distance of 436 ± 9.2 pc (Ortiz-León et al. (2017)). The bolometric temperature was calculating as described in Myers & Ladd (1993):

$$T_{bol} = 1.25\, 10^{-11}\, \bar{\nu} \tag{A.2}$$

where $\bar{\nu}$ is the mean frequency given by:

$$\bar{\nu} = \frac{\int \nu F_\nu d\nu}{\int F_\nu d\nu} \tag{A.3}$$

Using Scipy *splrep* and *splev* functions cubic smooth spline interpolation of the photometric data was performed while calculating the protostars parameters. Integration along the resulting axis was obtain with the composite trapezoidal rule (*Scipy* package). The photometric data allows us to perform the integration along wide range of wavelength with exception of SMM8. Here we have only 4 photometric points from the Herschel Gould Belt so the calculeted bolometric luminosity and temperature can be underestimated.

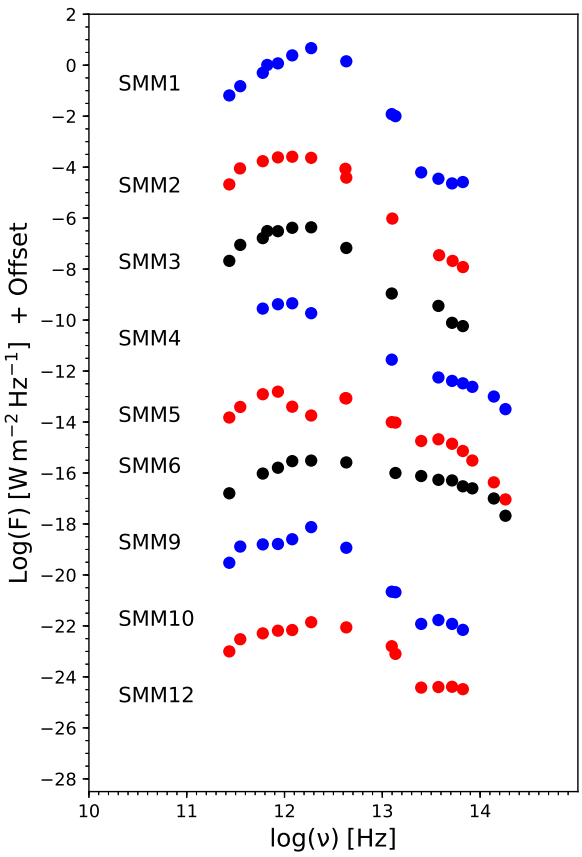

Fig. A.1. Spectral Energy Distributions of protostars in the Serpens Main region.

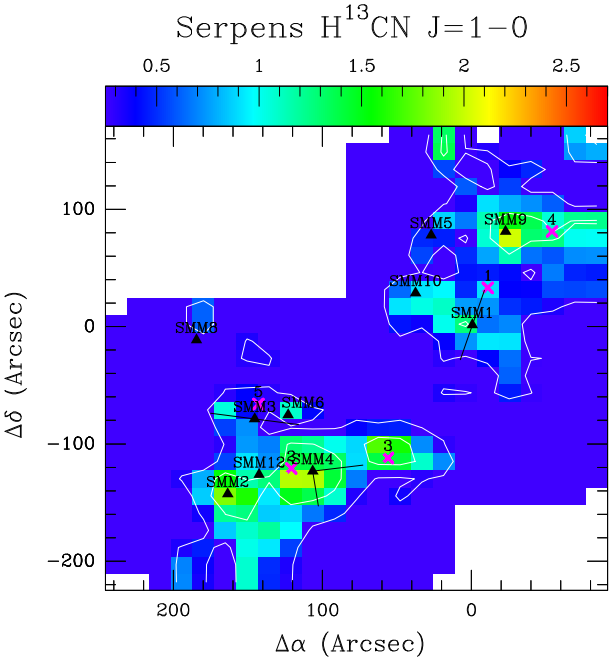

Fig. A.1. Similar to Fig. 2 but the emission of the $H^{13}CN$ $J = 1 - 0$ line.

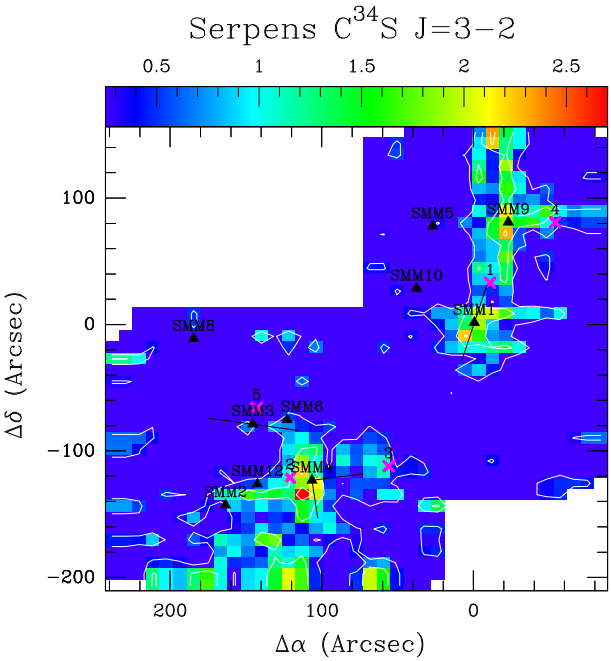

Fig. A.2. Similar to Fig. 2 but the emission of the $C^{34}S$ $J = 3 - 2$ line.

Appendix A: Molecular emission maps